

Band Calculations for Ce Compounds with AuCu₃-type Crystal Structure on the basis of Dynamical Mean Field Theory I. - CePd₃ and CeRh₃ -

Osamu SAKAI*

National Institute for Materials Science, Sengen 1-2-1, Tsukuba 305-0047, Japan

(Received April 19, 2010)

Band calculations for Ce compounds with the AuCu₃-type crystal structure were carried out on the basis of dynamical mean field theory (DMFT). The auxiliary impurity problem was solved by a method named NCA f^2 vc (noncrossing approximation including the f^2 state as a vertex correction). The calculations take into account the crystal-field splitting, the spin-orbit interaction, and the correct exchange process of the $f^1 \rightarrow f^0, f^2$ virtual excitation. These are necessary features in the quantitative band theory for Ce compounds and in the calculation of their excitation spectra. The results of applying the calculation to CePd₃ and CeRh₃ are presented as the first in a series of papers. The experimental results of the photoemission spectrum (PES), the inverse PES, the angle-resolved PES, and the magnetic excitation spectra were reasonably reproduced by the first-principles DMFT band calculation. At low temperatures, the Fermi surface (FS) structure of CePd₃ is similar to that of the band obtained by the local density approximation. It gradually changes into a form that is similar to the FS of LaPd₃ as the temperature increases, since the $4f$ band shifts to the high-energy side and the lifetime broadening becomes large.

KEYWORDS: dynamical mean field theory, band theory, ARPES, magnetic excitation, CePd₃, CeRh₃, Cauchy integral

1. Introduction

Nonempirical band calculations for strongly correlated electron systems have been extensively developed on the basis of dynamical mean field theory (DMFT).^{1,2)} The $4f$ electrons in Ce compounds are typical strongly correlated electrons.³⁻⁵⁾ Recently, a DMFT band calculation scheme for Ce compounds was developed in refs. 6 and 7. In the present work, it is applied to Ce compounds with the AuCu₃-type crystal structure, which show a wide variety of $4f$ electronic states from the most itinerant limit to the localized limit.

The $4f$ state splits into the $j = 5/2$ ground multiplet and the $j = 7/2$ excited multiplet with a separation of about 0.3 eV owing to the spin-orbit interaction (SOI). The multiplet shows crystal-field splitting (CFS) of the order of 100 K. In cubic crystals, the $j = 5/2$ multiplet splits into the $(j = 5/2)\Gamma_7$ doublet and the $(j = 5/2)\Gamma_8$ quartet. Hereafter, we call them the Γ_7 and Γ_8 states, respectively. It is important to take account of the SOI and CFS effects in $4f$ systems.³⁾ In DMFT, the correlated band electron problem is mapped onto the calculation of the single-particle excitation spectrum of the auxiliary impurity Anderson model in an effective medium. Reliable methods of solving the impurity Anderson model with CFS and the SOI effect are needed in the DMFT band calculation for $4f$ compounds. A theory named NCA f^2 vc (noncrossing approximation including the f^2 state as a vertex correction) has been developed⁸⁻¹¹⁾ and combined with the linear muffin-tin orbital (LMTO) method^{12,13)} to carry out the DMFT band calculation.⁷⁾ NCA f^2 vc can include CFS and the SOI effect, and also the correct exchange process of the

$f^1 \rightarrow f^0, f^2$ virtual excitation. The calculation gives an accurate order of the Kondo temperature (T_K).

The DMFT band calculation will be applied in a series of studies to Ce compounds with the AuCu₃-type structure: CePd₃, CeRh₃, CeIn₃, and CeSn₃. Each of these materials is classified as a typical example of strongly correlated $4f$ systems.^{5,14-19)}

CePd₃ is a typical heavy Fermion system with T_K of about 250 K, and has been studied extensively by various methods.^{5,18-31)} It has a nonmagnetic Fermi liquid (FL) ground state at low temperatures. A controversy existed in the experimental works on inelastic magnetic excitation, but it has recently been resolved by a detailed study of the wave number vector (wave vector) dependence of spectra.^{19,21-23)} The wave-vector-integrated-spectrum of the magnetic excitation has a broad peak at approximately 55 meV. In the single-particle excitation, a broad peak with the $4f$ character was observed on the inverse photoemission spectrum (IPES) side (i.e., in the energy region above the Fermi energy (E_F)). This seems to be consistent with the high T_K of this compound.²⁴⁻²⁷⁾ However, a strong peak structure has never been observed on the photoemission spectrum (PES) side (i.e., in the energy region below E_F), contradicting other physical properties.^{28,29)} Recent careful study using the $3d$ - $4f$ high-resolution resonant photoemission spectrum (RPES) revealed that the bulk component of the PES of this compound shows strong intensity at E_F consistently with high T_K .³⁰⁾ The angle-resolved PES (ARPES) has also been studied recently.³¹⁾ It may be worthwhile whether to confirm these recent results of studies are reproduced or not by the first-principles DMFT band calculation. CeRh₃ is known as one of the compounds having the most itinerant $4f$ states.^{25,26,32-36)}

*E-mail address: sakai_ym@star.ocn.ne.jp

CeSn₃ is also known to show the nonmagnetic FL ground state with a high characteristic temperature.^{37,38} CeIn₃ has an antiferromagnetic ground state with a Neel temperature of $T_N = 11$ K. Recently, it was found that T_N decreases to zero under the pressure of 2.5 GPa, in addition, the transition to superconductivity occurs at $T_{SC} = 0.2$ K.^{39–41} It will be interesting to study the change of the band structure under pressures by the DMFT calculation.

These compounds commonly have the AuCu₃-type crystal structure, which is classified into the simple cubic (*sc*) lattice. The DMFT band structure of these compounds will be reported in two papers. In CePd₃ and CeRh₃, the hybridization of *4f* states with *4d* states of the transition metal is very strong. The *4d* states almost sink to below E_F in CePd₃ whereas they are located near E_F in CeRh₃.⁴² In this paper, calculations for these *4d* compounds will be reported. Calculations for CeSn₃ and CeIn₃ will be given in a subsequent paper. Their *4f* states hybridize with broad *5p* states of ligand ions.

Calculated results of CePd₃ and CeRh₃ generally show reasonable agreement with experimental results of the PES, IPES, ARPES, and inelastic magnetic excitation by neutrons. However, the calculation gives a higher T_K than that expected from experiments when it is examined in detail. The DMFT band calculation for CePd₃ gives a Fermi surface (FS) structure similar to that obtained by the local density approximation (LDA) calculation at very low temperatures. When the temperature increases, *4f* bands shift to the high-energy side and their lifetime broadening increases. This leads to the change of the FS structure into one that is similar to the FS of LaPd₃. At $T = 150$ K, the FS has a different form from both FSs of LaPd₃ and the LDA band of CePd₃ as an intermediate stage of the change. The lifetime broadening overcomes the fine wave vector dependence of the *4f* spectrum at $T = 300$ K. In CeRh₃, the *4f* band is located at about 0.9 eV above E_F , and the dispersion of the DMFT band is almost identical to that of the LDA band in the energy region near E_F . The density of states (DOS) has an appreciable value slightly below E_F in the ARPES. This low-binding energy part shows a weak wave vector dependence, though no flat bands do not exist in the vicinity of the Fermi energy.

In §2, we briefly give the formulation on the basis of the LMTO method. Results of the application to CePd₃ are shown in §3, and results for CeRh₃ are given in §4. A summary is given in §5. In the appendices, notes on the calculation of the total electron number are given. An efficient method of calculating the Cauchy integral using the spline interpolation scheme is also presented. This integral is frequently used in the DMFT calculation.

2. Formulation

The method of calculation is described briefly because its details have been given in previous papers.^{6,7} We consider the excitation spectrum of the following Hamil-

tonian:

$$\mathcal{H} = \mathcal{H}_{\text{LDA}} + \frac{U}{2} \sum_{\mathbf{i}} \left(\sum_{\Gamma, \gamma} c_{\phi^a \mathbf{i} \Gamma \gamma}^+ c_{\phi^a \mathbf{i} \Gamma \gamma} - n_{\mathbf{i} f}^{\text{LDA}*} \right)^2. \quad (1)$$

Here, $c_{\phi^a \mathbf{i} \Gamma \gamma}$ is the annihilation operator for the atomic localized state $\phi_{\mathbf{i} \Gamma \gamma}^a(\mathbf{r})$ at site \mathbf{i} with the γ orbital of the Γ -irreducible representation. The quantity $n_{\mathbf{i} f}^{\text{LDA}*}$ is determined using the occupation number of the atomic *4f* electron per Ce ion in the LDA calculation. We assume that the local Coulomb interaction acts only on the orbital $\phi_{\mathbf{i} \Gamma \gamma}^a$.

The excitation spectrum is expressed by introducing the self-energy terms,⁶⁾

$$\mathcal{H}_{\text{DMFT}} = \mathcal{H}_{\text{LDA}} + \sum_{\mathbf{i}, (\Gamma, \gamma)} (\Sigma_{\Gamma}(\varepsilon + i\delta) + \varepsilon_{\Gamma}^a - \varepsilon_{\Gamma}^{\text{LDA}}) |\phi_{\mathbf{i} \Gamma \gamma}^a \rangle \langle \phi_{\mathbf{i} \Gamma \gamma}^a|, \quad (2)$$

where ε_{Γ}^a is the single-electron energy level of the *4f* state, and $\varepsilon_{\Gamma}^{\text{LDA}}$ is the energy level in the LDA calculation. The self-energy $\Sigma_{\Gamma}(\varepsilon + i\delta)$ is calculated by solving the auxiliary impurity problem with the use of NCA,^{f2vc}; its outline is described in the Appendix of ref. 7.

In later calculations we will approximate the localized *4f* state ϕ^a by the band center orbital $\phi(-)$ because its localization is good for the *4f* state. $\phi(-)$ has the logarithmic derivative $-\ell - 1$ on the muffin-tin surface.^{12,13)}

In the LMTO method, the Hamiltonian \mathcal{H}_{LDA} is diagonalized using the LMTO bases,

$$\psi^{j\mathbf{k}}(\mathbf{r}) = \sum_{qL} a_{qL}^{j\mathbf{k}} \chi_{qL}^{\mathbf{k}}(\mathbf{r}). \quad (3)$$

Here, $a_{qL}^{j\mathbf{k}}$ is the expansion coefficient of the *j*th eigenvector on the LMTO base of the Bloch type, $\chi_{qL}^{\mathbf{k}}(\mathbf{r})$, with the wave number vector \mathbf{k} , the angular momentum (ℓ, m) , and the spin (α) at site q in the unit cell, where $L \equiv (\ell, m, \alpha)$.¹³⁾

The explicit expression of $\chi_{qL}^{\mathbf{k}}(\mathbf{r})$ has been given in a previous paper.⁶⁾ Note that they are not orthogonal to each other, but the eigenvectors $\psi^{j\mathbf{k}}$ are orthonormal.

The DMFT band structure is calculated in the following way: (A) first the LDA part of the Hamiltonian \mathcal{H}_{LDA} is diagonalized for a given \mathbf{k} , (B) then the matrix equation of the Greenian is prepared in the manifold of the eigenvectors $\psi^{j\mathbf{k}}$. The Greenian equation for the given \mathbf{k} is written as

$$[zI - D_{\text{LDA}}(\mathbf{k}) - \Sigma(z)]G(z; \mathbf{k}) = I, \quad (4)$$

where I is the unit matrix and $D_{\text{LDA}}(\mathbf{k})$ is the diagonal matrix of the eigenenergies of \mathcal{H}_{LDA} with \mathbf{k} . The matrix elements of $\Sigma(z)$ are given by calculating the self-energy operator term of eq. (2) based on eq. (3).

The DOS on the atomic *4f* state is given by

$$\rho_{\Gamma}^{(\text{band})}(\varepsilon; \mathbf{k}) = -\frac{1}{\pi} \Im \text{tr}[\hat{O}_{\Gamma} G(\varepsilon + i\delta; \mathbf{k})], \quad (5)$$

where the projection operator is defined as

$$\hat{O}_\Gamma = \sum_{\mathbf{i} \gamma} |\phi_{\mathbf{i}}^a(\Gamma_\gamma)\rangle \langle \phi_{\mathbf{i}}^a(\Gamma_\gamma)|. \quad (6)$$

The local DOS in the DMFT band calculation is obtained by summing $\rho_\Gamma^{(\text{band})}(\varepsilon; \mathbf{k})$ over \mathbf{k} in the Brillouin zone: $\rho_\Gamma^{(\text{band})}(\varepsilon) = \frac{1}{N} \sum_{\mathbf{k}} \rho_\Gamma^{(\text{band})}(\varepsilon; \mathbf{k})$.⁴³ Here, N is the total number of unit cells.

The auxiliary impurity problem is solved by the NCA f^2 vc method. The splitting of the self-energy due to the SOI and CFS effects is considered. As shown in ref. 7, this method gives an accurate order of the Kondo temperature when the result is compared with that of the more correct numerical renormalization group (NRG) calculation^{7,44} in a simple model case.

Since the method of the self-consistent calculation in the DMFT has been described previously,^{6,7} we exclude the detailed explanation from this paper. First of all, we calculate the self-consistent LDA band by the LMTO method, and potential parameters, except for the f levels, are fixed to those in the LDA calculation. (I) We calculate the atomic $4f$ density of states $\rho_\Gamma^{(\text{imp.})}(\varepsilon)$ ($4f$ DOS) for the auxiliary impurity Anderson model by the NCA f^2 vc method with a trial energy dependence of the hybridization intensity (HI) and $4f$ levels,⁴⁵ then calculate the local self-energy. (II) The DMFT band calculation is carried out using the self-energy term, and the local $4f$ DOS in the DMFT band is calculated. The calculation is iterated so that the $4f$ DOS of the local auxiliary impurity model and the DMFT band satisfy the self-consistent conditions.^{46,47}

The $4f$ level is adjusted in the DMFT self-consistent iterations under the condition that the $4f$ occupation number has a given target value, $n_f(\text{rsl.target})$, which is estimated from the LDA band calculation. The temperature dependence of the Fermi energy, E_F , is neglected by fixing it at a value determined at a low temperature. It is estimated using the occupation number of the renormalized band (RNB) calculation, in which the self-energy is approximated by an expansion form up to the linear term in the energy variable at E_F (see Appendix A for the calculation of the total occupation number). The target $4f$ electron number $n_f(\text{rsl.target})$ is imposed on the occupation number calculated directly using the resolvents to stabilize the self-consistency iterations. The occupation number obtained by the integration of the $4f$ DOS, $n_f(\text{intg.})$, has a deviation within 1.0% from $n_f(\text{rsl.target})$ because many intermediate calculation process are included.

3. CePd₃

3.1 Density of states

In Fig. 1, we show the DOS of the $4f$ component ($4f$ DOS) for CePd₃ at $T = 37.5$ K. The solid line shows the total $4f$ component of the PES ($4f$ PES). The dashed line is the DOS of the Γ_7 component and the dot-dash line is the DOS of the Γ_8 component. The two-dots-dash line is the DOS of the $j = 7/2$ component. The CFS of the self-energy in the excited $j = 7/2$ multiplet is neglected. The vertical dot-dash line indicates the Fermi

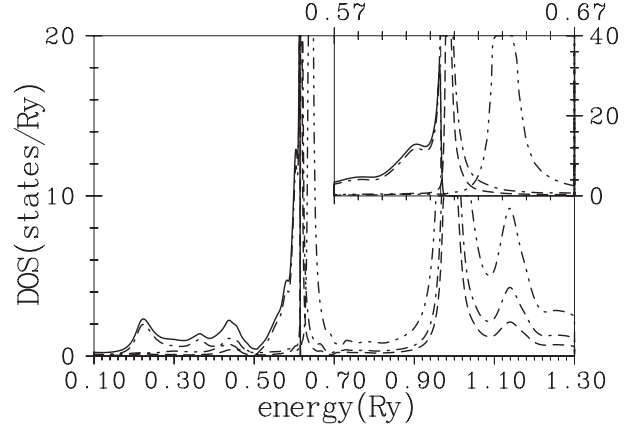


Fig. 1. $4f$ DOS of CePd₃ at $T = 37.5$ K. The solid line shows the total $4f$ PES. The dashed line is the DOS of the $(j = 5/2)\Gamma_7$ component, the dot-dash line is the DOS of the $(j = 5/2)\Gamma_8$ component, and the two-dots-dash line is the DOS of the $j = 7/2$ component. The Fermi energy $E_F = 0.6143$ Ry is indicated by the vertical dot-dash line. The inset shows spectra in the vicinity of E_F .

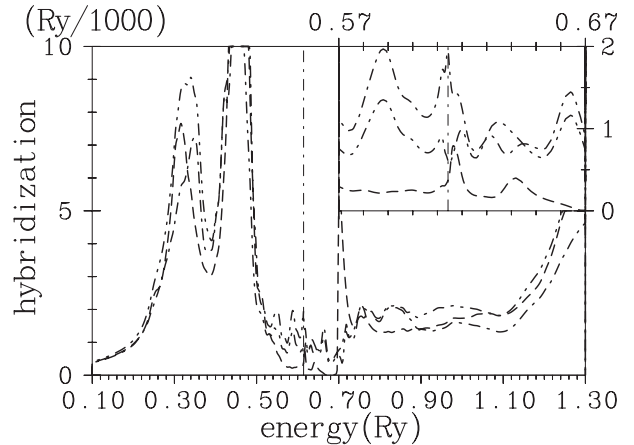


Fig. 2. Hybridization intensity (HI)⁵⁴ of CePd₃ at $T = 37.5$ K. The dashed line is the HI of the $(j = 5/2)\Gamma_7$ component, the dot-dash line is the HI of the $(j = 5/2)\Gamma_8$ component, and the two-dots-dash line is the HI of the $j = 7/2$ component. E_F is indicated by the vertical dot-dash line. The inset shows HI in the vicinity of E_F .

energy $E_F = 0.6143$ Ry. The inset shows spectra in the energy region near E_F . The $4f$ DOS has a large peak at 0.642 Ry, about 0.028 Ry (0.38 eV) above E_F . This has mainly the $j = 7/2$ character. The spin-orbit splitting on the IPES side is usually enhanced in Ce systems. The spectral intensity on the PES side consists mostly of the Γ_8 component. The PES has a sharp peak at E_F with a steep tail up to 0.094 Ry (1.3 eV) below E_F . It also has a long tail with small structures reflecting the DOS of $4d$ states of Pd on the high-binding-energy side. In the steep tail region, shoulders appear at binding energies of 0.004 Ry (0.05 eV) and 0.024 Ry (0.33 eV). These may correspond, respectively, to the CFS and the SOI side band. The sharp peak at E_F with the steep and the long tail has been observed in high-resolution experiments by Kasai *et al.*³⁰ The shoulder due to the SOI seems to be

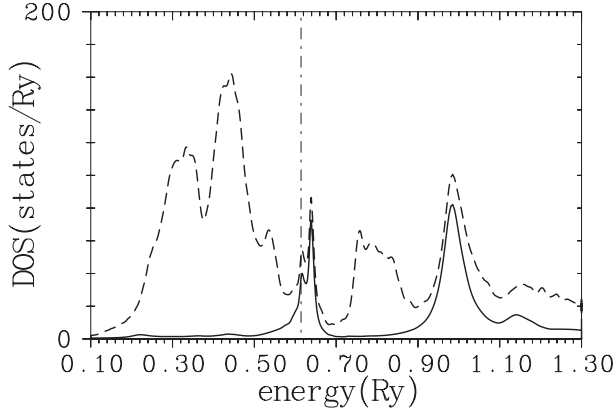


Fig. 3. Total DOS (dashed line) and 4f DOS (solid line) of CePd₃ at $T = 37.5$ K. The spectra are broadened by an imaginary factor, $\gamma = 0.01$ Ry, in the energy variable. E_F is indicated by the vertical dot-dash line.

Table I. Various quantities obtained in the DMFT calculation for CePd₃ at $T = 18.75$ K. $n_\Gamma^{(\text{imp.})}$ is the occupation number in the auxiliary impurity problem of the effective HI of the DMFT calculation, ε_Γ is the energy level in Ry. $\rho_\Gamma(E_F)$ is the partial DOS at E_F in Ry^{-1} . $\bar{Z}_\Gamma^{-1} = 1 - \partial \Re \Sigma_\Gamma(\varepsilon) / \partial \varepsilon|_{E_F}$ is the mass renormalization factor of the 4f band, $\bar{\varepsilon}_\Gamma$ is the effective energy of the renormalized band in Ry, and $\bar{\Gamma}_\Gamma$ is the imaginary part of the self-energy in Ry. The effective energy levels are measured from the Fermi energy $E_F = 0.6143$ Ry. The lattice constant is $a = 7.80079$ a.u., and the spin-orbit interaction constant is $\zeta_{4f} = 7.2302 \times 10^{-3}$ Ry. The 4f level in the band calculation is $\varepsilon_{4f}^{\text{LDA}} = 0.6754$ Ry. The electrostatic CFS of $(j = 5/2)\Gamma_7$ is set to be $\Delta E_{\Gamma 7} (= \varepsilon_{\Gamma 7}^a - \varepsilon_{\Gamma 8}^a) = 150$ K. The target 4f occupation number is $n_f(\text{rsl.target}) = 0.98$, and the resultant occupation number calculated using the resolvent is 0.980. The 4f occupation number calculated by integrating the spectra is $n_f(\text{intg.}) = 0.989$, and the obtained total band electron number is $N(\text{total; RNB}) = 34.006$. E_{inel} is the characteristic energy of the quasi-elastic excitation and E_{CFS} is the CFS excitation energy estimated from the magnetic excitation spectrum. The occupation number of the 4f state in CePd₃ in LDA is $n_f(\text{Ce, LDA}) = 1.045$. The Coulomb constant U is set to be 0.51 Ry (6.9 eV).⁴⁵⁾

	Γ_7	Γ_8	$j = 7/2$
$n_\Gamma^{(\text{imp.})}$	0.084	0.719	0.185
$\varepsilon_\Gamma(\text{Ry})$	-0.19027	-0.19182	-0.16493
$\rho_\Gamma(E_F)(\text{Ry}^{-1})$	3.8	59.0	0.5
\bar{Z}_Γ^{-1}	6.3	6.7	3.6
$\bar{\varepsilon}_\Gamma(\text{Ry})$	0.0153	0.0057	0.1184
$\bar{\Gamma}_\Gamma(\text{Ry})$	2.7×10^{-4}	16.0×10^{-4}	3.0×10^{-4}
$E_{\text{inel}} = 27$ meV, $E_{\text{CFS}} = 41$ meV			

identified.

The Kondo temperature T_K and the CFS excitation energy are, respectively, estimated to be about 27 meV (310 K) and 41 meV (480 K) from magnetic excitation spectra, as will be shown in Fig. 4 in the next subsection. We note that spectra do not show appreciable change even when the temperature is decreased to 18.75 K in the calculation.

The parameters and the calculated values are given in Table I. The LMTO band parameters¹³⁾ for states except for the f component are fixed to those of the LDA

calculation. E_F is fixed to the value determined by the occupied state in the RNB, as is discussed in a later section. The relative occupation number of the Γ_7 component to the Γ_8 , 0.084/0.719 (0.12) is small compared with the 0.5 expected from the ratio of the degeneracy, but is very large compared with the value expected from the simple model of the CFS for an isolated ion with $\varepsilon_{\Gamma 7} - \varepsilon_{\Gamma 8} = 0.00155$ Ry (240 K). The ratio does not change so greatly even when the temperature is raised: 0.089/0.723 (0.12) at 150 K and 0.108/0.707 (0.15) at 300 K. Moreover, the occupation of the $j = 7/2$ component, 0.185, is not small, and is almost independent of T . A simple picture of the CFS for an isolated ion cannot be applied.

Usually, the electrostatic potential causes cubic CFS in 4f electron systems with a higher energy level of about 150 K for the Γ_7 state.^{48,49)} This is included in the present calculation. Even when it is neglected, the 4f DOS and the magnetic excitation spectrum are not greatly changed because the hybridization effect causes large CFS, of greater than 300 K.⁵⁰⁾

The target value of the occupation number on the atomic 4f states, $n_f(\text{rsl.target})$, has been tentatively chosen to be 0.98 in the present calculation. This value is small compared with the 4f occupation number, 1.045, of the LDA band calculation for CePd₃. When we carry out the LDA calculation for compounds in which Ce ions are replaced by La ions, the occupation number on the 4f(La) state usually amounts to 0.1.⁵¹⁾ We use the occupation number as reduced to 94% of the LDA value as the atomic occupation number on the Ce 4f state. Kanai *et al.* concluded that 4f occupancy in CePd₃ is expected to be 0.92 on the basis of the results of resonant inverse photoemission (RIPES) experiments.^{27,52,53)} When we perform the DMFT band calculation by setting $n_f(\text{rsl.target})$ to be 0.92, T_K determined from the magnetic excitation spectrum is expected to be 500 K. On the other hand, T_K is greatly reduced to about 10 K when we choose 1.05.

In Fig. 2, we show the trial HI⁵⁴⁾ obtained in the DMFT band calculation at 37.5 K. It has very large peaks corresponding to the 4d band of Pd, but these peaks are located in the energy region deep below E_F . The HI is not high in the energy region near E_F . In particular, the HI of the Γ_7 component is low though it is high in the deeper energy region. The overall features of the HI in the DMFT band are similar to those calculated directly using the LDA band, but the HI in DMFT is increased in the vicinity of E_F to about twice the LDA value for the Γ_7 and Γ_8 components, and is decreased in the deep energy region. Moreover, the DMFT calculation causes fine structures of the HI in the vicinity of E_F , which are shown in the inset of the figure. This contrasts with the HI in the LDA, which has a weak energy dependence in this region. The HI of the Γ_8 component in DMFT has a small peak at E_F , while those of the Γ_7 and $j = 7/2$ components have small peaks above or on both sides of E_F . The reason for this different behavior is not clear at present, but we note that the peaks of the 4f DOS for the latter two cases are located above

E_F . When we do a calculation in the fictitious case that Γ_7 is mainly occupied by assigning a low energy level to it, the HI of Γ_7 has a small peak at E_F . However, this result should not be used as a general rule, because the modification of HI in DMFT is delicately dependent on details of the band structures. The Kondo temperature is increased in the DMFT calculation in the CePd₃ case. We have obtained the Kondo temperature of 10 K in the single impurity calculation using the HI of the LDA band.

The total DOS at $T = 37.5$ K is shown by the dashed line in Fig. 3. The large peaks at about 0.3 and 0.45 Ry have the 4d character of Pd, and that at 0.8 Ry has the 5d character of Ce. These peaks are also obtained by the LDA calculation.⁵⁵⁾ The sharp 4f peaks slightly above E_F , which are called the f^1 peak in IPES, are also obtained in the LDA calculation.⁴²⁾ Their intensity in DMFT is reduced compared with that in the LDA because a part of it is transferred to the intensity of the peak at about 1.0 Ry, which is called the f^2 peak. In the present calculation, the width of the f^2 peak is not large because the multiplet splitting of the f^2 final state is neglected.

In the analysis of RIPES experiments, the ratio of the f^1 peak to the total RIPES intensity has been given as 0.22,²⁷⁾ whereas it is estimated to be about 0.2 in the present calculation. The present DMFT calculation seems to give results that emphasizes the hybridization effects strongly (i. e. the higher T_K).

3.2 Magnetic excitation

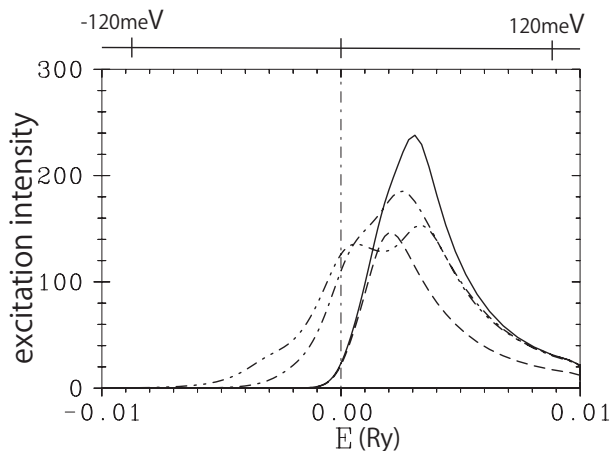


Fig. 4. Magnetic excitation spectrum of CePd₃. The solid line shows the spectrum at $T = 37.5$ K, the dot-dash line is the spectrum at $T = 150$ K, and the two-dots-dash line is the spectrum at $T = 300$ K. The dashed line is the spectrum in a fictitious case where matrix elements of the magnetic moment are restricted within the intra- Γ_8 manifold of space.

In Fig. 4 we show the magnetic excitation spectrum. The total magnetic excitation spectrum at $T = 37.5$ K is shown by the solid line. It has a peak at about $E = 0.003$ Ry (41 meV). The dashed line depicts the spectrum for a

fictitious case in which the matrix elements of the magnetic moment are nonzero only in the manifold of Γ_8 , and thus it may correspond to the excitation spectrum within the Γ_8 manifold. It has a peak at about $E = 0.002$ Ry (27 meV), and leads to a faint shoulder in the solid line. The CFS excitation energy seems to be slightly larger than T_K in the present calculation. The calculated magnetic susceptibility is 1.9×10^{-3} emu/mol, whereas the experimental value is 1.5×10^{-3} emu/mol at $T \sim 0$ K.^{56,57)} We show magnetic excitation spectra at $T = 150$ K and at $T = 300$ K by the dot-dash line and the two-dots-dash line, respectively. The spectrum at $T = 300$ K has a broad peak centered at about 0.003 Ry (41 meV). The shoulder shifts to $E \sim 0$ and becomes a peak. The overall features do not change so greatly when we neglect the electrostatic CFS of 150 K. The magnetic excitation spectrum observed in the wave-vector-integrated case has a peak at about 55 meV at $T = 10$ K, and the peak shifts to the low-energy side as T increases.²¹⁾ The calculated results seem to be generally consistent with those of the experiment. However, the peak at $E \sim 0$ is higher at $T = 300$ K in the experiments.²¹⁾ The present DMFT calculation seems to give stronger HI compared with the value in the experiments. The detailed calculation of physical quantities using finely tuned parameters will be given in the future.

In ref. 22, excitation peaks with an energy of 15 meV and less than 3 meV are indicated. Low-energy peaks are not expected in the present calculation of the wave-vector-integrated spectra because T_K is not low. One possibility of the origin of the low-energy peaks may be the wave vector dependence of the magnetic excitation spectra, as noted in ref. 23.

3.3 RNB, and wave number-vector-dependent DOS

In Fig. 5, we show the RNB dispersion at $T = 37.5$ K. The energy shift (the real part of the self-energy at E_F : $\Re\Sigma_\Gamma(E_F)$) and the mass renormalization factor ($1 - \partial\Re\Sigma_\Gamma(\varepsilon)/\partial\varepsilon|_{E_F}$), which are given in Table I, are taken into account in this calculation. Narrow bands with the $j = 5/2$ character appear slightly above E_F , and those with the character of $j = 7/2$ appear around the energy 0.645 Ry which is near the energy of the $j = 7/2$ peak in the 4f DOS shown in Fig. 1.

The lowest 4f band sinks to below E_F near the Γ and R points, and is located above E_F in the other regions. The dispersion of RNB corresponds well with the behavior of the \mathbf{k} -dependent density of states (k-DOS). For example, we show the k-DOS when \mathbf{k} moves from the Γ (bottom) to the R (top) point along the Λ line in Fig. 6. A peak of the DOS with mainly the 4f character is located below E_F at the Γ and R points. Starting from the peak below E_F at the Γ point, one of ridge lines runs above the Fermi energy across E_F , and then connects to the peak below E_F at the R point. Another runs to the low-energy side of E_F up to 0.611 Ry at the halfway, and then turns back to connect to the peak below E_F at the R point. This “hanging” branch does not cross the Fermi energy.

Note that we have depicted the total spectral intensity, not the f -component, in Fig. 6. In the energy region

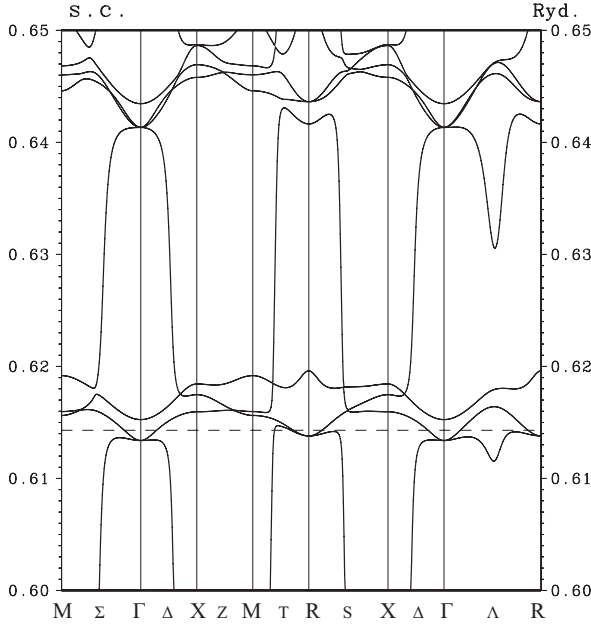


Fig. 5. Band dispersion of the renormalized band (RNB) picture for CePd_3 at $T = 37.5$ K. The symbols under the horizontal axis denote the symmetry points and axes of the Brillouin zone of the sc lattice. E_F is indicated by the horizontal dashed line.

shown in the figure, the spectral intensity has mainly the $4f$ character. On the other hand, very sharp spectral peaks of a non- $4f$ character appears in the energy region outside of the figure. The hanging band on the Λ axis has a stronger non- $4f$ character. This branch is a hybridization band between the $4f$ of Ce and a conduction band that has the character of the sp -free electron band and the $5d$ of Ce.

The dispersion of the RNB is qualitatively similar to the result of the band structure determined by Hasegawa and Yanase by the LDA calculation,⁵⁸⁾ although the width of the $4f$ band with $j = 5/2$ is about 0.005 Ry in the RNB, whereas that of the LDA band is about 0.02 Ry. Both calculations give electron pockets at the Γ and R points, and hole pockets centered on the T axis.⁵⁹⁾

The Main features of the band dispersion near the Fermi energy are formed by the hybridization of the narrow $4f$ bands and the wide sp bands. The $4f$ bands have dispersion characterized by the LMTO (linear combination of atomic orbitals) tight-binding bands of the sc lattice. Although the $4f$ band width is reduced in DMFT, the qualitative features of the dispersion of the $4f$ - sp hybridized bands are not changed because the number of

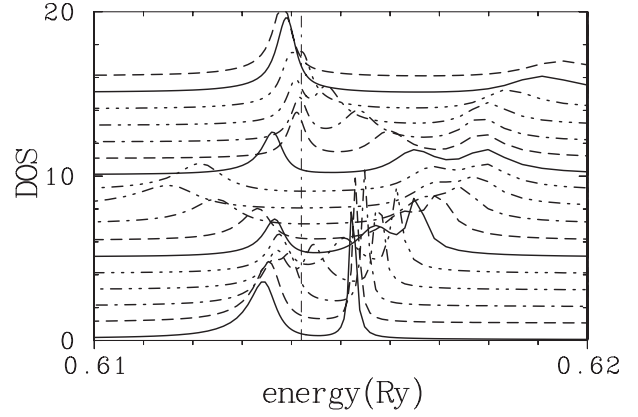


Fig. 6. Wave number vector (\mathbf{k}) dependence of the DOS (k -DOS) for CePd_3 at $T = 37.5$ K. \mathbf{k} is moved from the Γ point (bottom) to the R point (top) along the Λ axis. The total DOS is shown, but the $4f$ component is dominant in this energy region of CePd_3 .

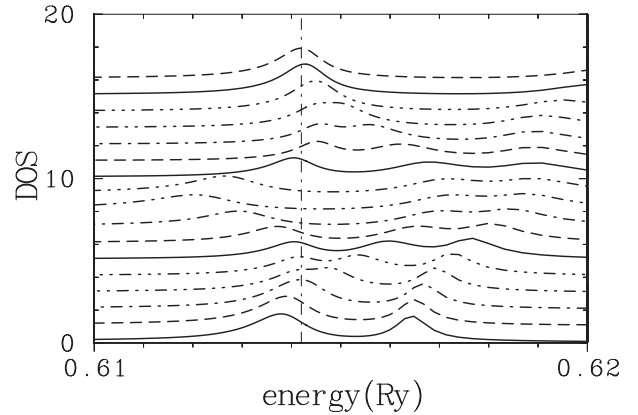


Fig. 7. k -DOS of CePd_3 at $T = 150$ K. \mathbf{k} is changed from the Γ point (bottom) to the R point (top) along the Λ axis.

participating sp bands is small and their dispersion is very rapid compared with that of $4f$ bands.

Here, we must note a weak point of the $\text{NCA}f^2\text{vc}$ method, that is it does not automatically ensure the Fermi liquid sum rule, i.e., the integral of the total DOS below E_F , $N(\text{total}; \rho) = \int d\varepsilon \frac{1}{N} \sum_{\mathbf{k}} (-\frac{1}{\pi} \Im G(\varepsilon + i\delta; \mathbf{k})) f(\varepsilon)$, is not equal to the occupation number of electrons calculated by the volume of the occupied states in the \mathbf{k} space. The quantity $N(\text{total}; \rho)$ is a smaller value in CePd_3 , and thus we obtain a higher Fermi energy. If we use it in the RNB calculation, the volume of the occupied states in the \mathbf{k} space becomes large. In the case of CePd_3 , which has an even total electron number, the balance between the electron and hole states is lost. In this study, we tentatively use the Fermi energy determined using the quantity $N(\text{total}; \text{RNB}) = \frac{1}{N} \sum_{\lambda \mathbf{k}} f(E_{\text{RNB}}(\lambda \mathbf{k}))$ to ensure the electron-hole balance in the RNB band, where $E_{\text{RNB}}(\lambda \mathbf{k})$ is the energy obtained by the RNB calculation. (For more details, see Appendix B.)

When we calculate the RNB dispersion at $T = 150$ K, the $4f$ band shifts slightly to the high-energy side. The $4f$ state at the Γ point nears E_F , and the $4f$ state at

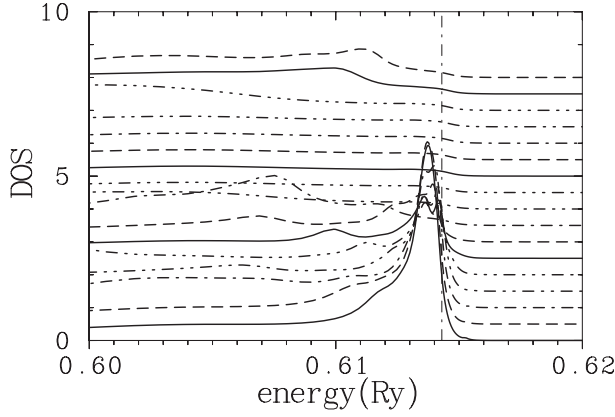


Fig. 8. Angle-resolved PES of CePd₃ at $T = 37.5$ K. The surface is assumed to be (111). The representative \mathbf{k} is swept from the Γ (bottom) point to the M (top) point along the Σ axis, and the intensities are averaged over the wave number vector normal to the (111) surface. This means that \mathbf{k} also runs from the R (bottom) point to the X (top) point along the S axis. The Fermi energy E_F is indicated by the vertical dot-dash line. The total DOS is shown, but the intensity above the energy of 0.612 Ry is dominated by the 4f character. The intensity below 0.611 Ry has mainly the non-4f character.

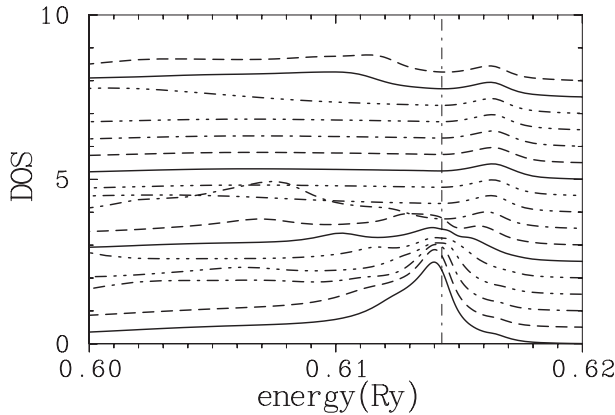


Fig. 9. Angle-resolved PES of CePd₃ at $T = 150$ K. For the definition of lines, see the caption of Fig. 8.

the R point is located on E_F . Therefore, a part of the hanging band on the Λ line rises above E_F . Hole pockets on the T axis grow into larger hole regions around the R point. As the temperature increases further, the 4f state at the R point shifts up to above E_F , and a large hole surface enclosing the R point appears. In other words, we have a connected electron Fermi surface (FS) that contains the X and M points inside it.

The primary structure of the FS of the RNB at high temperatures is similar to that of the FS of the LDA band of LaPd₃, but their fine topologies will differ. At $T = 150$ K, the main part of the hanging band on the Λ line is still located below E_F . The hole sheets around the Γ and R points are separated by an electron region on the Λ axis. On the other hand, this entire hanging branch is located above E_F in LaPd₃, and thus the separation by the electron region does not occur.

We should, of course, note that the RNB picture has

only limited meaning at high temperatures because the imaginary part is large.⁶⁰⁾ The k-DOS at $T = 150$ K for \mathbf{k} along the Λ line is shown in Fig. 7. The widths of peaks become large, but we can see that the peak at the R point is located almost at E_F , and the peak at Γ nears E_F . The trace of broad peaks shows a shift corresponding to that of the RNB dispersion. We can recognize that the ridge of the peaks of the hanging band crosses the Fermi energy, as noted in the previous paragraph. At $T = 300$ K, the width of peaks becomes so large that it surpasses the fine \mathbf{k} dependence of the spectra. However, the 4f peak near the Fermi energy still exists in the 4f DOS calculation, similar to that shown in Figs. 1 and 3. It moves slightly to the high-energy side with increasing width at 300 K.

The present calculation has been performed with fixed E_F and $n_f(\text{rsl.target})$. The calculated total occupation number in the DMFT band increases to $N(\text{total}; \text{RNB}) = 34.304$ at $T = 300$ K, although the energies of the 4f bands shift upward.⁶¹⁾ We point out that even when we move E_F , the energy of 4f bands relative to the Fermi energy will not change greatly because the Kondo resonance peak usually shifts following the change of the Fermi energy.

Recently, the wave vector dependence of the PES has been observed under the 4d \rightarrow 4f resonant condition.³¹⁾ The experiment was carried out for the (111) surface of a thin film by sweeping the \mathbf{k} vector along $\bar{\Gamma}\text{-}\bar{K}\text{-}\bar{M}\text{-}\bar{K}\text{-}\bar{\Gamma}$ in the surface Brillouin zone (BZ). This may correspond to the following sweeping of \mathbf{k} in the 3-dimensional sc BZ: the component parallel to the surface runs as $\Gamma\text{-(}\Sigma\text{)-M-(}\Sigma\text{)-}\Gamma$ with averaging over its components normal to the surface. This means that the sweeping of the parallel component R-(S)-X-(S)-R is also included.

In Fig. 8, we show the PES when the representative wave vector moves from the Γ (bottom) point to the M (top) point with average intensities for \mathbf{k} normal to the surface. The total intensity is plotted in the figure, but the intensity above the energy of 0.612 Ry has mainly the 4f character. The spectra have a peak for \mathbf{k} near Γ , and this corresponds well to the experimental results. The intensity below the energy of 0.611 Ry has a non-4f character. As noted previously, the contribution from the R point is also included at the representative Γ point. At these points, the 4f component is located below E_F at $T = 37.5$ K. In Fig. 9, we show spectra at $T = 150$ K. The peak of the intensity at Γ nears E_F because of the shifting up of the 4f band. The thermal distribution effect and the very high intensity of the 4f DOS above E_F also have affect this spectral shape. The change of the peak can be checked in experiments.

4. CeRh₃

In Fig. 10, we show the 4f DOS of CeRh₃ at 10³ K. The 4f spectrum has a sharp and large peak at an energy about of 0.76 Ry, which is 0.066 Ry (0.9 eV) above the Fermi energy. This separation of energy from E_F is slightly smaller than that of the 4f band in the LDA, about 0.009 Ry (1.2 eV). The result seems to be consistent with those of RIPES experiments and their detailed analysis.^{26,32)} The PES has a relatively large peak at

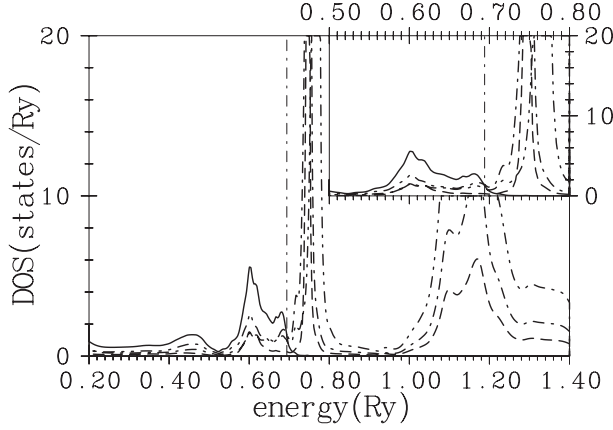


Fig. 10. 4f DOS of CeRh₃ at $T = 10^3$ K. For the definition of lines, see the caption of Fig. 1. $E_F = 0.6940$ Ry is indicated by the vertical dot-dash line.

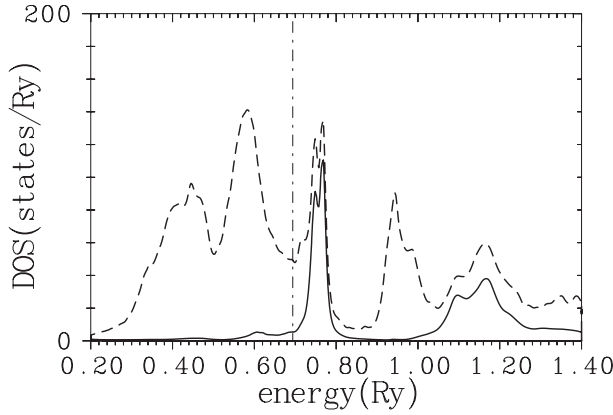


Fig. 11. Total DOS (dashed line) and 4f DOS (solid line) of CeRh₃ at $T = 10^3$ K. See the caption of Fig. 3.

about 0.1 Ry (1.4 eV) below E_F and a peak at E_F . The qualitative behavior of the present PES is similar to the result obtained by Harima in the LDA.⁶²⁾ However, the binding energy of the peak at 0.1 Ry below E_F is slightly lower and the intensity is higher than that of the LDA. The peak at E_F is also slightly sharper. In the experiment, the sharp peak at E_F was observed, but the peak at 0.1 Ry below E_F has not been identified at present.^{33–36)}

In Fig. 11, we show the total and 4f DOS of CeRh₃ at $T = 10^3$ K. The 4d band of Rh exhibits strong peaks of the DOS at about 0.4 and 0.6 Ry. The 4f component also has a small peak at about 0.6 Ry, as noted previously. The Fermi energy is located in the top region of the 4d band, and the hybridization intensity in this region is high. Dispersions of the RNB are almost identical to those of the LDA in the energy region very near E_F , but the width of the 4f band, which is located at 0.76 Ry, is about 2/3 that of the LDA. A f^2 satellite peak appears in DMFT at about 1.2 Ry on the high-energy side. The ratio of the intensity of peak at 0.76 Ry (f^1 peak) to the total IPES intensity is estimated to be about 0.4 in the present calculation, while a slightly larger value, 0.6, was obtained in the experiment. Uozumi *et al.* pre-

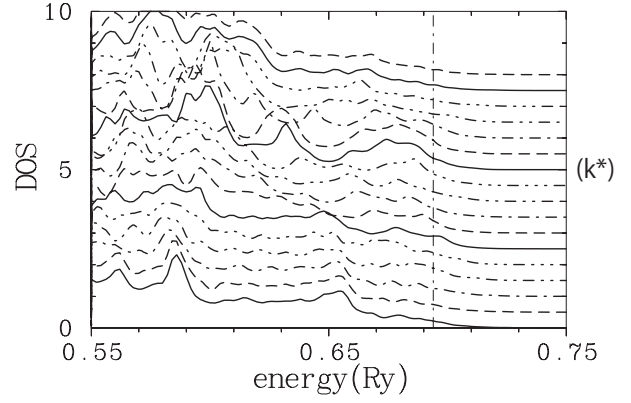


Fig. 12. Angle-resolved PES of CeRh₃ at $T = 300$ K. For the definition of lines, see the caption of Fig. 8. The \mathbf{k} point corresponding to the second solid line from the top is named \mathbf{k}^* in the text.

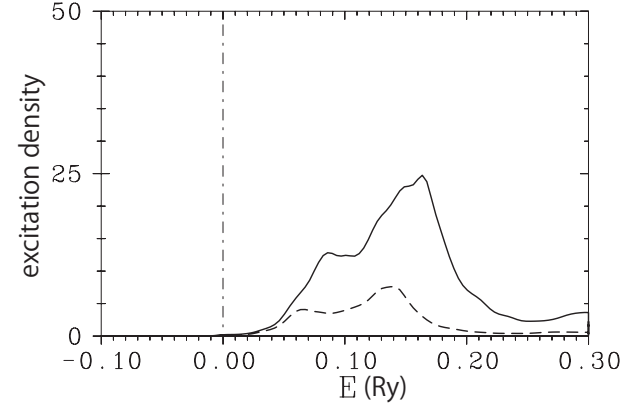


Fig. 13. Magnetic excitation spectra of CeRh₃ at $T = 10^3$ K. The solid line is the total intensity and the dashed line is the result calculated using a fictitious model in which the matrix elements of the magnetic moment are restricted within the $j = 5/2$ manifold of states.

dicted the 4f occupation number to be 0.86,³²⁾ but we tentatively used $n_f(\text{rsl.target}) = 0.94$, which is 94% of the LDA value. The difference between these values is not small, but will not cause extreme differences in the calculation of the very strong hybridization limit. The mass enhancement factor is expected to be about 2, as given in Table II.

In Fig. 12, we show the PES for the (111) surface when the representative wave vector moves from the Γ point (bottom) to the M point (top). In the energy region between E_F and 0.6 Ry, the relative intensity of the 4f component is about 10% of the total. The spectra have fine peaks as if some flat bands exist slightly below E_F . However, we note that no flat bands exist very near E_F in the RNB dispersion. Let us denote as \mathbf{k}^* the representative \mathbf{k} corresponding to the second solid line from the top (i.e., the \mathbf{k} point on the Σ axis at a distance of about $0.3 \times$ length of the Σ axis from the M point). The spectral intensity slightly below E_F is relatively large for \mathbf{k} near \mathbf{k}^* . For the wave vectors near \mathbf{k}^* , several bands stay

Table II. Various quantities obtained in the DMFT calculation for CeRh₃ at $T = 10^3$ K. For the definition of notation, see the caption of Table I. The Fermi energy is $E_F = 0.6940$ Ry and $\Delta E_7 = 0$ K. The lattice constant is $a = 7.6005$ a.u., and the spin-orbit interaction constant is $\zeta_{4f} = 7.3374 \times 10^{-3}$ Ry. The $4f$ level in the band calculation is $\varepsilon_{4f}^{\text{NCA}} = 0.7639$ Ry. The target $4f$ occupation number is $n_f(\text{rsl.target}) = 0.94$, and the resultant occupation number calculated using the resolvent is 0.940. The $4f$ electron number calculated by the integrating the spectra is $n_f(\text{intg.}) = 0.943$, and the obtained total band electron number is $N(\text{total; RNB}) = 30.994$. $n_f(\text{Ce, LDA}) = 0.996$.

	Γ_7	Γ_8	$j = 7/2$
$n_{\Gamma}^{(\text{imp.})}$	0.178	0.319	0.446
$\varepsilon_{\Gamma}(\text{Ry})$	-0.26923	-0.26921	-0.24426
$\rho_{\Gamma}(E_F)(\text{Ry}^{-1})$	0.27	1.40	0.99
Z_{Γ}^{-1}	2.2	1.9	1.9
$\bar{\varepsilon}_{\Gamma}(\text{Ry})$	0.1218	0.1216	0.1646
$\bar{\Gamma}_{\Gamma}(\text{Ry})$	4.6×10^{-3}	12.6×10^{-3}	5.8×10^{-3}
$E_{\text{inel}} = 0.03$ Ry			

slightly below E_F around the M and X points when the normal components are varied. Calculated results show quantitatively similar behaviors to experimental results, but the careful separation of the surface and bulk components is necessary to enable a detailed comparison.⁶³⁾

The magnetic excitation spectra are shown in Fig. 13. They have a steep increase at the excitation energy of about 0.03 Ry. This energy may correspond to the energy from E_F to the low-energy edge of the peak at 0.76 Ry of the $4f$ DOS. The low energy end of the spectrum mainly originates from the excitation within the $j = 5/2$ components, but contribution of the $j = 7/2$ components is not small even in the low-excitation-energy region. The $j = 7/2$ components also join the Kondo effect. We may expect the Kondo temperature of this system to be about 0.03 Ry (4700 K). The calculated value of the magnetic susceptibility is 0.7×10^{-4} emu/mol. The experimental magnetic susceptibility ($\chi \sim 4 \times 10^{-4}$ emu/mol)⁵⁷⁾ may indicate a high T_K of several thousand K, but the calculated value of 4700 K seems to be too high. DOSs, both of the total and of the $4f$ component, do not have any gap, as seen in Fig. 10, but the magnetic excitation spectrum has a shape indicating the existence of a pseudogap. We note that, in Fig. 13, the excitation spectra of only intra- $4f$ components are shown. A broad continuous $5d$ component will be superposed on these spectra.

The HI of CeRh₃ in the LDA calculation has a spectrum shape similar to that of the partial DOS on the $5d$ state of Rh, i.e., the spectral shape given by subtracting the $4f$ and $5d$ parts of the Ce ion from the total DOS in Fig. 11. The HI in DMFT is almost equal to that of the LDA in the high-energy region, but it has a steep dip at an energy slightly above E_F . Similar behavior has been seen in the HI of the $j = 7/2$ component of CePd₃ which has shown in Fig. 2.

5. Summary and Discussion

We have studied the electronic structures of CePd₃ and CeRh₃ on the basis of the DMFT calculation. The auxiliary impurity problem was solved by a method named NCA f^2 vc, which includes the correct exchange process

of the $f^1 \rightarrow f^0$ and $f^1 \rightarrow f^2$ virtual excitation. The splitting of the self-energy owing to the SOI and CFS effects was also considered.

The DMFT band calculation gives Fermi surface structures similar to those obtained by the LDA calculation in CePd₃⁵⁸⁾ at very low temperatures. Electron pockets appear at the bottom of the $4f$ band at the Γ and R points. Hole pockets appear that are centered on the T symmetry axis.

The $4f$ band shifts to the high-energy side relative to the Fermi energy as the temperature increases. At the same time, the lifetime width of the $4f$ states increases. The band structures produced by the band overlap between the $4f$ and non- $4f$ components shift up to the high energy side of the Fermi energy. Therefore the primary structures of the band in the vicinity of the Fermi energy approaches to those of the sp free-electron-like band of LaPd₃. However, some characteristic features of the LDA band of CePd₃ remain at higher temperatures. For example, a region that electrons occupy will appear on the Λ axis in CePd₃ at $T \sim 150$ K, which is not expected in LaPd₃. In CePd₃, the lifetime broadening overcomes the \mathbf{k} dependence of the $4f$ spectrum at room temperature, thus, the $4f$ state becomes a broad dispersionless state located above E_F .

The ARPES of CePd₃ shows strong intensity near the representative Γ point at low temperatures because the $4f$ band is located below the Fermi energy at the Γ and R points. This result seems to be consistent with the recent experimental results.³¹⁾ The observed $4f$ component will be greatly reduced at room temperature because of the shift of the $4f$ band to the high-energy side.

The \mathbf{k} -integrated magnetic excitation spectrum has a peak at 41 meV and a faint shoulder structure at about 27 meV at low temperatures. The temperature dependence of the excitation spectrum generally seems to be consistent with the results of experiments.²¹⁾ The magnetic CFS excitation energy is estimated to be about 41 meV, while the Kondo temperature is slightly smaller, 320 K (27 meV).

The calculated PES shows good correspondence with the bulk component obtained in recent high-resolution experiments.³⁰⁾ The intensity ratio of the f^1 peak of the IPES to the total IPES is estimated to be about 0.2, while it was predicted to be 0.22 by the recent experiment analysis.²⁷⁾ The HI is enhanced near the Fermi energy in the DMFT band compared with that of the LDA calculation. The present DMFT calculation seems to give electronic structures with slightly stronger HI than that expected from experiments for CePd₃.

The DMFT calculation for CeRh₃ gives an almost identical band structure to that obtained by the LDA calculation. However, the energy of the f^1 peak of the IPES in the former is slightly lower than that in the latter. In addition, the f^2 satellite peak appears in the DMFT band calculation. The calculated intensity ratio of the f^1 peak to the total IPES, 0.4, is comparable to, but smaller than the experimental value of 0.6.³²⁾ The calculated PES has a sharp peak at the Fermi energy. A peak reflecting the $4d(\text{Rh})$ DOS also appears, simi-

larly to the result of the LDA calculation. The former has been observed, but the latter has not been identified in experiments.^{35,36)}

The Fermi energy is located in the energy region of the $4d$ band of Rh in CeRh_3 , therefore the HI near the Fermi energy is strong, about three times greater than that of CePd_3 . The $4f$ band width of CeRh_3 is about twice that of CePd_3 in the LDA calculation. In the DMFT calculation, the characteristic energy scales are drastically different from each other, 300 and 5000 K.

In CeRh_3 , the ARPES shows an appreciable DOS slightly density below the Fermi energy and is weakly dependent on the wave vector, although no flat $4f$ bands exist near the Fermi energy in the RNB dispersion. The spectra have stronger intensity halfway along the Σ axis from the Γ to M points of the Brillouin zone. This seems to be similar to the results of experiments, but further studies to separate the surface effects are necessary.⁶³⁾

General features of the experimental results for CePd_3 and CeRh_3 are reproduced by the DMFT band calculation with the LMTO+NCA f^2 vc scheme. However, the present DMFT calculation gives a higher Kondo temperature than that in the results of the detailed analysis of experiments. Moreover, there is some arbitrariness in the choice of the target value of the $4f$ occupation number, $n_f(\text{rsl.target})$. According to calculations for AuCu₃-type Ce compounds, accurate calculated results seem to be obtained when a $4f$ occupation number between 90% and 95% of the LDA value is used. We have used 94% in the present calculation, and we obtained 310 K (27 meV) for T_K of CePd_3 ($n_f(\text{rsl.target}) = 0.98$) and 4700 K (0.03 Ry) for T_K of CeRh_3 ($n_f(\text{rsl.target}) = 0.94$) from the magnetic excitation spectrum. When we perform calculations using 90%, the T_K are 400 K for CePd_3 ($n_f(\text{rsl.target}) = 0.94$) and 6300 K for CeRh_3 ($n_f(\text{rsl.target}) = 0.90$). These values are not greatly different from the previous values because these compounds belong to a group of materials having high T_K . For materials with lower T_K , T_K drastically depends on the choice of $n_f(\text{rsl.target})$. Careful treatment of the target value is necessary in such cases.

The effectiveness and some of the weaknesses (for example, the correct calculation of the occupied electron number) of the present DMFT scheme are recognized. Calculations of the $4f$ band state in CeIn_3 and CeSn_3 , and also various Ce compounds will be carried out in the near future.

At the end of this paper, we refer the very early and recent application of methods similar to NCA f^2 vc to the DMFT band calculation. Lægsgaard and Svane calculated the band structure of Ce pnictides in 1998.⁶⁴⁾ Recently, Haule *et al.* studied the $\alpha \rightarrow \gamma$ transition of Ce metal,⁶⁵⁾ and Shim *et al.* studied the electronic band structure of CeIrIn_5 .⁶⁶⁾ The CFS of the self-energy was not considered in those studies.

Acknowledgments

The author would like to thank H. Shiba for encouragements, and Y. Kuramoto and J. Otsuki for important comments on the resolvent method, H. Harima for valu-

able comments on the band calculation method, and Y. Shimizu for valuable collaboration in the early stage of developing the LMTO+NCA f^2 vc code. This work was partly supported by Grants-in-Aid for Scientific Research C (No. 21540372) from JSPS, and on Innovative Areas “Heavy Electrons” (No. 21102523) and for Specially Promoted Research (No. 18002008) from MEXT.

Appendix A: Occupation number

The calculation based on the NCA f^2 vc method usually does not satisfy the FL sum rule, i.e., the integral of the total DOS below the Fermi energy, $N(\text{total}; \rho) = \int d\varepsilon \frac{1}{N} \sum_{\mathbf{k}} (-\frac{1}{\pi} \Im G(\varepsilon + i\delta; \mathbf{k})) f(\varepsilon)$, is not equal to the value $N(\text{total}; \ln G) = \int d\varepsilon \frac{1}{N} \sum_{\mathbf{k}} (-\frac{1}{\pi} \Im \ln \det G(\varepsilon + i\delta; \mathbf{k})) (-\frac{\partial f(\varepsilon)}{\partial \varepsilon})$, where $f(\varepsilon)$ is the Fermi distribution function at $T = 0$. In the RNB calculation, in which the self-energy term is approximated by $\Sigma_{\Gamma}(z) \approx \Re \Sigma_{\Gamma}(E_F) + \frac{\partial \Re \Sigma_{\Gamma}(z)}{\partial z} |_{E_F} (z - E_F)$, we obtain real eigen energies $E_{\text{RNB}}(\lambda \mathbf{k})$ where λ is the band suffix. The number of occupied states in the RNB band, $N(\text{total}; \text{RNB}) = \frac{1}{N} \sum_{\mathbf{k}} f(E_{\text{RNB}}(\lambda \mathbf{k}))$, is expected to agree with $N(\text{total}; \ln G)$ at $T = 0$ if the imaginary part can be neglected near the Fermi energy. However, the imaginary component has a considerable magnitude in NCA f^2 vc even at very low temperatures; this is partly because T must maintain the condition $T \gtrsim 0.1T_K$. For example, $N(\text{total}; \rho)$, $N(\text{total}; \ln G)$, and $N(\text{total}; \text{RNB})$ are 33.59, 34.16, and 34.01, respectively, at $T = 18.75$ K in CePd₃. The difference between these values becomes serious when the detailed structure of the Fermi surface is discussed. In this study, we use $N(\text{total}; \text{RNB})$ to determine the Fermi energy E_F at $T = 0$ because this quantity is directly related to the occupation number of electrons calculated from the volume of the occupied states in the \mathbf{k} space.

Appendix B: Cauchy integral of using spline interpolation

The Cauchy integral appears in various places in the DMFT calculation. Therefore, an efficient and accurate numerical calculation of the Cauchy integral is needed. We briefly explain a method of using the spline interpolation for the DOS. Let us assume that numerical data of DOS $\{y_i\}$ at energy points $\{x_i\}$ ($i = 1, N_{\text{datanumber}}$) are given. In the cubic spline interpolation,⁶⁷⁾ the DOS in the interval $[x_i, x_{i+1}]$ is expressed as

$$\rho_{3,i}(x) = \frac{1}{6h_i} \{(x_{i+1} - x)^3 M_i + (x - x_i)^3 M_{i+1}\} + (y_i - \frac{h_i^2 M_i}{6}) \frac{x_{i+1} - x}{h_i} + (y_{i+1} - \frac{h_i^2 M_{i+1}}{6}) \frac{x - x_i}{h_i}, \quad (\text{B} \cdot 1)$$

where $h_i = x_{i+1} - x_i$. The quantity M_i is the second derivative of the DOS at $x = x_i$, and is given by the usual procedure of the spline interpolation.

The integral of the interval $[x_i, x_{i+1}]$ is calculated as

$$\begin{aligned} \int_{x_i}^{x_{i+1}} \frac{\rho_{3,i}(x)}{z - x} dx &= (x_{i+1} - z)^2 \frac{M_i}{6} - (z - x_i)^2 \frac{M_{i+1}}{6} \\ &+ (x_{i+1} - z) \frac{M_i h_i}{12} - (z - x_i) \frac{M_{i+1} h_i}{12} \\ &+ (y_i - \frac{h_i^2 M_i}{9}) - (y_{i+1} - \frac{h_i^2 M_{i+1}}{9}) \\ &- \rho_{3,i}(z) \ln \frac{z - x_{i+1}}{z - x_i}. \end{aligned} \quad (\text{B} \cdot 2)$$

The total integral is given by summing the contribution from each interval. Equation (B-2) is expressed as a com-

bination of powers of quantities $(x_{i+1} - z)$ and $(z - x_i)$; therefore it is applicable for z when $|z - \frac{x_i + x_{i+1}}{2}|$ is not much larger than h_i . When z approaches the edge of the integration, i.e., $z \rightarrow x_i$ or x_{i+1} , the singularity of the logarithm term is removed by the counter contribution of the neighboring $[x_{i-1}, x_i]$ or $[x_{i+1}, x_{i+2}]$ region. The round-off error due to the subtraction of logarithm terms of neighboring regions is not serious even when z is extremely near the edge point, because the divergence of the logarithm is very weak. The integral (B-2) is expected to be $O(z - \frac{x_i + x_{i+1}}{2})^{-1}$ when $|z - \frac{x_i + x_{i+1}}{2}| \gg h_i$. Therefore, mutual cancellation occurs among terms in (B-2) in this limit. We find that the integral is re-expressed by a compact form in this case

$$\begin{aligned} &\int_{x_i}^{x_{i+1}} \frac{\rho_{3,i}(x)}{z - x} dx \\ &= - \sum_{\nu=1}^{\infty} [(\frac{h_i}{x_{i+1} - z})^{\nu} (\frac{y_i}{\nu + 1} - \frac{h_i^2 M_i}{3(\nu + 3)(\nu + 1)}) \\ &\quad - (\frac{h_i}{z - x_i})^{\nu} (\frac{y_{i+1}}{\nu + 1} - \frac{h_i^2 M_{i+1}}{3(\nu + 3)(\nu + 1)})]. \end{aligned} \quad (\text{B} \cdot 3)$$

This equation gives a highly accurate estimation of the integral even when terms are truncated up to $\nu \sim 10$.

In most cases, it is convenient to use the linear interpolation scheme with a very fine mesh for the DOS,

$$\rho_{1,i}(x) = m_i(x - \frac{x_i + x_{i+1}}{2}) + \frac{y_i + y_{i+1}}{2}, \quad (\text{B} \cdot 4)$$

where $m_i = \frac{y_{i+1} - y_i}{h_i}$. The Cauchy integral is expressed by the following forms

$$\int_{x_i}^{x_{i+1}} \frac{\rho_{1,i}(x)}{z - x} dx = -m_i h_i - \rho_{1,i}(z) \ln \frac{z - x_{i+1}}{z - x_i}, \quad (\text{B} \cdot 5)$$

and for $|z - \frac{x_i + x_{i+1}}{2}| \gg h_i$,

$$\begin{aligned} \int_{x_i}^{x_{i+1}} \frac{\rho_{1,i}(x)}{z - x} dx &= -\frac{1}{2} \sum_{\nu=1}^{\infty} [(\frac{h_i}{x_{i+1} - z})^{\nu} (\frac{y_{i+1}}{\nu} - \frac{m_i h_i}{\nu + 1}) \\ &\quad - (\frac{h_i}{z - x_i})^{\nu} (\frac{y_i}{\nu} - \frac{m_i h_i}{\nu + 1})]. \end{aligned} \quad (\text{B} \cdot 6)$$

- 1) K. Held, I. A. Nekrasov, G. Keller, V. Eyert, N. Blümer, A. K. McMahan, R. T. Scalettar, T. Pruschke, V. I. Anisimov, and D. Vollhardt: *phys. Status Solidi B* **243** (2006) 2599.
- 2) L. V. Pourovskii, B. Amadon, S. Biermann, and A. Georges: *Phys. Rev. B* **76** (2007) 235101.
- 3) A. C. Hewson: *The Kondo Problems to Heavy Fermions* (Cambridge University Press, Cambridge, 1993)
- 4) J. W. Allen: *J. Phys. Soc. Jpn.* **74** (2005) 34.
- 5) J. C. Parlebas and A. Kotani: *J. Electron Spectrosc. Relat. Phenom.* **136** (2004) 3.
- 6) O. Sakai, Y. Shimizu, and Y. Kaneta: *J. Phys. Soc. Jpn.* **74** (2005) 2517.
- 7) O. Sakai and Y. Shimizu: *J. Phys. Soc. Jpn.* **76** (2007) 044707.
- 8) O. Sakai, M. Motizuki, and T. Kasuya: *Core-Level Spectroscopy in Condensed Systems Theory*, ed. J. Kanamori and A. Kotani (Springer-Verlag, Berlin, 1988) p. 45.
- 9) J. Otsuki and Y. Kuramoto: *J. Phys. Soc. Jpn.* **74** (2006) 064707.
- 10) J. Kroha and P. Wölfle: *J. Phys. Soc. Jpn.* **74** (2005) 16.
- 11) For the resolvent method, see, for example, N. E. Bickers: *Rev. Mod. Phys.* **59** (1987) 845.
- 12) O. K. Andersen: *Phys. Rev. B* **12** (1975) 3060.

- 13) H. L. Skriver: *The LMTO Method* (Springer-Verlag, Berlin, 1984).
- 14) D. W. Lynch and J. H. Weaver: in *Handbook on Physics and Chemistry of Rare Earths*, ed. K. A. Gschneidner, Jr., L. Eyring, and S. H. Hüfner (Elsevier Science, Amsterdam, 1987) Vol. 10, p. 231.
- 15) F. U. Hillebrecht and M. Campagna: in *Handbook on Physics and Chemistry of Rare Earths*, ed. K. A. Gschneidner, Jr., L. Eyring, and S. H. Hüfner (Elsevier Science, Amsterdam, 1987) Vol. 10, p. 425.
- 16) Y. Ōnuki and A. Hasegawa: in *Handbook on Physics and Chemistry of Rare Earths*, ed. K. A. Gschneidner, Jr., and L. Eyring (Elsevier Science, Amsterdam, 1995) Vol. 20, p. 1.
- 17) M. R. Norman and D. D. Koelling: in *Handbook on Physics and Chemistry of Rare Earths*, ed. K. A. Gschneidner, Jr., L. Eyring, G. H. Lander, and G. R. Choppin (Elsevier Science, Amsterdam, 1993) Vol. 17, p. 1.
- 18) M. Loewenhaupt and K. H. Fisher: in *Handbook on Physics and Chemistry of Rare Earths*, ed. K. A. Gschneidner, Jr., and L. Eyring (Elsevier Science, Amsterdam, 1993) Vol. 16, p. 1.
- 19) E. Holland-Moritz and G. H. Lander: in *Handbook on Physics and Chemistry of Rare Earths*, ed. K. A. Gschneidner, Jr., L. Eyring, G. H. Lander, and G. R. Choppin (Elsevier Science, Amsterdam, 1994) Vol. 19, p. 1.
- 20) J. M. Lawrence, J. D. Thompson, and Y. Y. Chen: Phys. Rev. Lett. **54** (1985) 2537.
- 21) A. P. Murani, A. Servering, and W. G. Marshall: Phys. Rev. B **53** (1996) 2641.
- 22) S. M. Shapiro, C. Stassis, and G. Aeppli: Phys. Rev. Lett. **62** (1989) 94.
- 23) J. M. Lawrence, V. R. Fanelli, E. A. Goremychkin, R. Osborn, E. D. Bauer, K. J. McClellan, and A. D. Christianson: Physica B **403** (2008) 783.
- 24) M. Grioni, D. Malterre, P. Weibel, B. Dardel, and Y. Baer: Physica B **186-188** (1993) 38.
- 25) M. Grioni, P. Weibel, D. Malterre, Y. Baer, and L. Duò: Phys. Rev. B **55** (1997) 2056.
- 26) K. Kanai, Y. Tezuka, T. Terashima, Y. Muro, M. Ishikawa, T. Uozumi, A. Kotani, G. Schmerber, J. P. Kappler, J. C. Parlebas, and S. Shin: Phys. Rev. B **60** (1999) 5244.
- 27) K. Kanai, T. Terashima, A. Kotani, T. Uozumi, G. Schmerber, J. P. Kappler, J. C. Parlebas, and S. Shin: Phys. Rev. B **63** (2001) 033106.
- 28) R. D. Parks, S. Raaen, M. L. denBoer, and Y.-S. Chang: Phys. Rev. Lett. **52** (1984) 2176.
- 29) S. Ogawa, S. Suga, A. E. Bocquet, F. Iga, M. Kasaya, T. Kasuya, and A. Fujimori: J. Phys. Soc. Jpn. **62** (1993) 3575.
- 30) S. Kasai, S. Imada, A. Yamasaki, A. Sekiyama, F. Iga, M. Kasaya, and S. Suga: J. Electron Spectrosc. Relat. Phenom. **156-158** (2007) 441.
- 31) S. Danzenbächer, Yu. Kucherenko, M. Heber, D. V. Vyalikh, S. L. Molodtsov, V. D. Servedio, and C. Laubschat: Phys. Rev. B **72** (2005) 033104.
- 32) T. Uozumi, K. Kanai, S. Shin, A. Kotani, G. Schmerber, J. P. Kappler, and J. C. Parlebas: Phys. Rev. B **65** (2002) 045105.
- 33) E. Weschke, C. Laubschat, R. Ecker, A. Höhr, M. Domeke, and G. Kaindl: Phys. Rev. Lett. **69** (1992) 1792.
- 34) D. Malterre, M. Grioni, Y. Baer, L. Braicovich, L. Duò, P. Vavassori, and G. L. Olcese: Phys. Rev. Lett. **73** (1994) 2005.
- 35) R.-J. Jung, B.-H. Choi, S.-J. Oh, H.-D. Kim, E.-J. Cho, T. Iwasaki, A. Sekiyama, S. Imada, S. Suga, and J.-G. Park: Phys. Rev. Lett. **91** (2003) 157601.
- 36) Yu. Kucherenko, S. L. Molodtsov, and C. Laubschat: Phys. Rev. Lett. **94** (2005) 039709.
- 37) A. P. Murani: J. Phys. C: Solid State Phys. **33** (1983) 6359.
- 38) I. Umehara, Y. Kurosawa, N. Nagai, M. Kikuchi, K. Satoh, and Y. Ōnuki: J. Phys. Soc. Jpn. **59** (1990) 2848.
- 39) N. D. Mathur, F. M. Grosche, S. R. Julian, I. R. Walker, D. M. Freye, R. K. Haselwimmer, and G. G. Lonzarich: Nature **394** (1998) 39.
- 40) F. M. Grosche, I. R. Walker, S. R. Julian, N. D. Mathur, D. M. Freye, M. J. Steiner, and G. G. Lonzarich: J. Phys.: Condens. Matter **13** (2001) 2845.
- 41) R. Settai, H. Shishido, T. Kubo, A. Araki, T. C. Kobayashi, H. Harima, and Y. Ōnuki: J. Magn. Magn. Mater. **310** (2007) 541.
- 42) L. Severin and B. Johansson: Phys. Rev. B **50** (1994) 17886.
- 43) The summation over \mathbf{k} is carried out on a mesh dividing the $\Gamma-X$ axis into 8 parts. Usually this gives a nearly smooth spectrum for $4f$ components, but gives fictitious fine structures for non- $4f$ components. The total DOS is calculated by smoothing with the introduction of the imaginary part $\gamma = 0.01$ Ry in the energy variable.
- 44) O. Sakai, Y. Shimizu, and T. Kasuya: J. Phys. Soc. Jpn. **58** (1989) 3666.
- 45) In NCA f^2 vc, the atomic energy levels are treated as independent input parameters. The energy level of the f^0 state is $E(f^0) = 0$ and the energy level of the f^1 state is $E(f^1, \Gamma) = \varepsilon_\Gamma$ when levels are measured from E_F . The energy level of the f^2 state is assumed to be $E(f^2) = 2\varepsilon(f) + U$, where $\varepsilon(f) = \frac{1}{6}(2\varepsilon_{\Gamma_7} + 4\varepsilon_{\Gamma_8})$ is the average of f levels of the $j = 5/2$ multiplet, and U is the Coulomb constant.
- 46) The impurity $4f$ Green function is given using the $4f$ DOS $\rho_\Gamma^{(\text{imp.})}(x)$ as the Cauchy integral: $G_\Gamma^{(\text{imp.})}(z) = \int dx \frac{\rho_\Gamma^{(\text{imp.})}(x)}{z-x}$. It is also expressed as $G_\Gamma^{(\text{imp.})}(z) = 1/[z - \varepsilon_\Gamma^a - \Sigma_\Gamma(z) - \Sigma_\Gamma^{(h)}(z)]$, where ε_Γ^a is the impurity level, and $\Sigma_\Gamma(z)$ and $\Sigma_\Gamma^{(h)}(z)$ are, respectively, the self-energies due to the Coulomb interaction and the hybridization.⁶⁾ The self-energy $\Sigma_\Gamma(z)$ is calculated as $\Sigma_\Gamma(z) = z - \varepsilon_\Gamma^a - G_\Gamma^{(\text{imp.})}(z)^{-1} - \Sigma_\Gamma^{(h)}(z)$ by solving the impurity model with the HI $-\Im\Sigma_\Gamma^{(h)}(x+i\delta)$. The self-consistent condition on the $4f$ DOS in DMFT is $\rho_\Gamma^{(\text{imp.})}(x) = \rho_\Gamma^{(\text{band})}(x)$. Under the self-consistent condition, the self-energy due to the hybridization is given by $\Sigma_\Gamma^{(h)}(z) = z - \varepsilon_\Gamma^a - G_\Gamma^{(\text{imp.})}(z)^{-1} - \Sigma_\Gamma(z)$.
- 47) We find that the maximum relative difference of the $4f$ DOS hardly decreases below 0.5, even when we advance the iteration process. The average of the relative differences of the Greenian on the imaginary axis is monitored as the convergence parameter, but this also hardly decreases below 0.3×10^{-2} . We usually stop the iteration process when this parameter reaches approximately 0.3×10^{-2} and shows stationary behavior.
- 48) A. Furrer and H.-G. Purwins: J. Phys. C **9** (1976) 1491.
- 49) U. Walter and E. Holland-Moritz: Z. Phys. B: Condens. Matter **45** (1981) 107.
- 50) When the CFS of the electrostatic term is not included, a large number of iteration loops are needed to reach a solution for large CFS because the calculation starts with a condition of equal energy levels: $\varepsilon_{\Gamma_7}^a = \varepsilon_{\Gamma_8}^a$.
- 51) When we perform the LDA calculation for a fictitious LaPd₃ with the lattice constant of CePd₃, the occupation number on the $4f$ state is estimated to be 0.188, which is larger than that of usual compounds, about 0.1. This large occupation is induced through the strong hybridization between the $4f$ state and the $4d(\text{Pd})$ state located in the energy region deep below E_F . Some parts of the $4f$ occupation in LaPd₃ may be ascribed to the tail of the $4d(\text{Pd})$ extending to the Ce region.
- 52) Kasai *et al.* predicted the $4f$ occupation number to be 0.79 from their bulk PES analysis.³⁰⁾ However, they analyzed the PES using the NCA calculation and obtained a small occupation number because the f^2 configuration was neglected. For NCA, see, for example, refs. 11 and 53.
- 53) Y. Kuramoto: Z. Phys. B **53** (1983) 37.
- 54) Under the self-consistent condition, the self-energy due to the hybridization is given by $\Sigma_\Gamma^{(h)}(z) = z - \varepsilon_\Gamma^a - G_\Gamma^{(\text{imp.})}(z)^{-1} - \Sigma_\Gamma(z)$, where ε_Γ^a is the impurity level, $G_\Gamma^{(\text{imp.})}(z)$ is the impurity Green's function and $\Sigma_\Gamma(z)$ is the self-energy due to the Coulomb interaction. The HI shown in Fig. 2 is defined as $-\Im\Sigma_\Gamma^{(h)}(x+i\delta)$. This is the quantity corresponding to $\sum_{\nu\mathbf{k}} \pi |v_\Gamma(\nu\mathbf{k})|^2 \delta(x - E_{\nu\mathbf{k}})$ in the usual impurity problem, where $v_\Gamma(\nu\mathbf{k})$ is the $c-f$ hybridization matrix and $E_{\nu\mathbf{k}}$ is the energy of the band state.

- 55) C. Koenig: Z. Phys. B: Condens. Matter **50** (1983) 33.
- 56) R. M. Galera, A. P. Murani, J. Pierre, and K. R. A. Ziebeck: J. Magn. Magn. Mater. **63-64** (1987) 594.
- 57) T. Gambke, B. Elchner, J. Schaafhausen, and H. Schaeffer: *Valence Fluctuations in Solids*, ed. L. M. Falicov, W. Hanke, and M. B. Maple (North-Holland, Amsterdam, 1981) p. 447.
- 58) A. Hasegawa and A. Yanase: J. Phys. Soc. Jpn. **56** (1987) 3990.
- 59) The $4f$ electron occupation number calculated using the RNB is 0.84 at $T = 37.5$ K for CePd₃. This value is large compared with the value supposed from the impression of Fig. 5 in which only the bottoms of $4f$ bands are occupied. The $4f$ occupation number through the hybridization with conduction bands is considerable in the RNB picture of CePd₃. The LDA calculation also gives $4f$ bands where only their bottoms are occupied in the same way as in the RNB calculation, and leads to the $4f$ occupation number of 1.045.
- 60) The $4f$ DOS calculated by DMFT is shown in Fig. 1. The spectrum intensity in the deep region from E_F (“the incoherent component” in the terminology of band theory and “the f^0 excitation part” in the terminology of the local Kondo problem) has a considerably high intensity. However, this deep energy component is disregarded in RNB, but its intensity is recovered as the full value of the intensity of the “coherent part” in the calculation of the occupied state. Only the band dispersion in the neighborhood of E_F and the count of the occupied k states at very low temperatures compared with the Kondo temperature have meaning in the RNB calculation.
- 61) Note that the temperature dependence of $N(\text{total}; \rho)$ is not strong: it is 33.59 at $T = 18.75$ K, and is 33.60 at $T = 300$ K.
- 62) H. Harima: private communication. See Fig. 3 of ref. 35.
- 63) W. Schneider, S. L. Molodtsov, M. Richter, Th. Gantz, P. Englemann, and C. Laubschat: Phys. Rev. B **57** (1998) 14930.
- 64) J. Lægsgaard and A. Svane: Phys. Rev. B **58** (1998) 12817.
- 65) K. Haule, V. Oudovenko, S. Y. Savrasov, and G. Kotliar: Phys. Rev. Lett. **94** (2005) 036401.
- 66) J. H. Shim, K. Haule, and G. Kotliar: Science **318** (2007) 1618.
- 67) See for example, A. Ralston, and P. Rabinowitz: *A First Course in Numerical Analysis* (McGraw-Hill, New York, 1978) 2nd ed.